PyRiverShift: A Gaussian Transect Decomposition Framework for Quantifying Sub-Pixel Lateral Channel Mobility

Manudeo Singh* and Stephen Tooth

Department of Geography and Earth Sciences, Aberystwyth University, Wales, UK

**Corresponding Author: mas291@aber.ac.uk*

Keywords: *Gaussian sub-pixel fitting, fluvial remote sensing, geomorphology, Barotse floodplain, Zambezi River*

PyRiverShift: A Gaussian Transect Decomposition Framework for Quantifying Sub-Pixel Lateral Channel Mobility

Manudeo Singh and Stephen Tooth

Department of Geography and Earth Sciences, Aberystwyth University, Wales, UK · mas291@aber.ac.uk

***Abstract*—Along many rivers, lateral channel mobility is a key process, yet quantification from freely available multi-decadal 30 m Landsat imagery is constrained by low pixel resolution relative to channel width. We introduce PyRiverShift, a sensor-agnostic spectral decomposition framework. PyRiverShift fits a 1-D Gaussian to NDWI profiles along valley-perpendicular transects, recovering sub-pixel channel centre position with propagated uncertainty, FWHM width, and quality-flags, without binary water-masking or centreline extraction. A Bayesian Information Criterion (BIC) -guided two-Gaussian mixture model identifies secondary and/or abandoned channels. Applied to the 170 km upper Zambezi floodplain, PyRiverShift achieved median σ_pos = 6.0 m (IQR 5.0–7.8 m, n = 22,126). Statistically significant lateral mobility was detected (92% of transects), with median migration rate 3.1 m/yr (95% CI 2.8–3.4) from 1986-2025. Median FWHM width was 260 m (IQR 205–344 m). Positional uncertainty remains stable across threshold settings but increases 25% beyond 90 m ground sampling distance.**

***Index Terms*—*Gaussian sub-pixel fitting, fluvial remote sensing, geomorphology, Barotse floodplain, Zambezi River*

I. Introduction

Along many rivers, channel mobility resulting from lateral migration, bend cutoff, avulsion and/or width adjustments is a visible process of change, with the balance between erosion and deposition having implications for channel size and sinuosity trends, floodplain sediment residence times, riparian habitat dynamics, and infrastructural stability. Quantifying lateral mobility rates from the Landsat archive is now standard in fluvial geomorphology [1], [2], yet existing methods face a fundamental resolution barrier: channels narrower than ~90–150 m occupy no more than five pixels at 30 m Landsat resolution and cannot support a reliable binary water mask, placing them beyond current automated methods. For channels wide enough to be masked, centre position is localised to the nearest pixel edge, tying precision to pixel resolution. For the Landsat archive, this limitation means missing metre-scale mobility signals and precluding width trend detection in all but the largest rivers.

Several open tools automate channel extraction from water masks. RivMAP [3] quantifies meandering planform changes at annual resolution but requires channels wide enough to skeletonise (i.e. extract a single-pixel centreline from a binary mask) reliably (≥8 pixels, ~240 m). RivaMap [4] applies a multi-scale singularity index for centreline detection but inherits the same pixel-floor constraint. RivWidthCloud [5] extracts top-widths globally via Google Earth Engine but provides neither sub-pixel position nor positional uncertainty. The JRC Global Surface Water dataset [6] provides a 40-year pixel-resolution water occurrence record but does not resolve channel centreline or width at the sub-pixel level. A recent review [7] identifies sub-pixel position uncertainty quantification as an open methodological gap.

Gaussian or PSF (Point Spread Function) based convolutional models have been widely used in sub-pixel mapping and remote sensing image degradation frameworks, where the observed signal is treated as a blurred representation of an underlying fine-scale scene [8]. However, these formulations have rarely been extended to spatio-temporal river morphology tracking or channel evolution analysis under explicit uncertainty propagation.

This letter contributes: (i) a Gaussian sub-pixel fitting framework applied to NDWI [9] (extendable to any wetness index) transect profiles with covariance-derived positional uncertainty suitable for weighted regression; (ii) Bayesian Information Criterion (BIC)-based [10] two-Gaussian model selection identifying multi-thread reaches without empirical thresholds; and (iii) a demonstration on the upper Zambezi River where seasonal channel-floodplain inundation confounds pixel-level water masks. A temporal continuity window prevents false detections in competing off-channel water bodies. The implementation is open-source Python, compatible with xarray–geopandas and Google Earth Engine workflows via the xee backend, and supports parallel processing. Full implementation with demonstration using Jupyter Notebooks will be hosted at: https://github.com/manudeo/pyRiverShift.

II. Study Area and Data

The study reach encompasses ~170 km of the upper Zambezi River within the Barotse floodplain (also known as the Bulozi Plain), western Zambia (Fig. 1). The Zambezi is a low-gradient (~0.16 m km^{-1}), sand-bed, sinuous, dominantly single-thread channel, with a typical bankfull width of 80–350 m. Scroll plains and oxbows (Fig. 1c, f) attest to lateral mobility within a 10–50 km wide floodplain that is seasonally inundated for 4–6 months (normally Dec to Mar) by floods ranging between ~310 and 2319 m^3 s^{-1} at Senanga station [11], [12].

Despite being one of central southern Africa's major river systems, with the Barotse floodplain listed as a Ramsar Wetland of International Importance (Ramsar site no. 1662), the Zambezi's scale, topographic complexity, and hydrological variability preclude systematic ground surveys, making remote sensing the only practical means of quantifying lateral mobility. This setting tests our method's discrimination of narrow channel signal from spectrally similar seasonal floodwater. WetlandMapper [13], a python-based open-source software, was used to pre-process and calculate wetness index (NDWI) on Google Earth Engine. All cloud-free Landsat 5/7/8/9 surface reflectance images (USGS Collection 2, Level 2) from January 1986 through December 2025 were used.

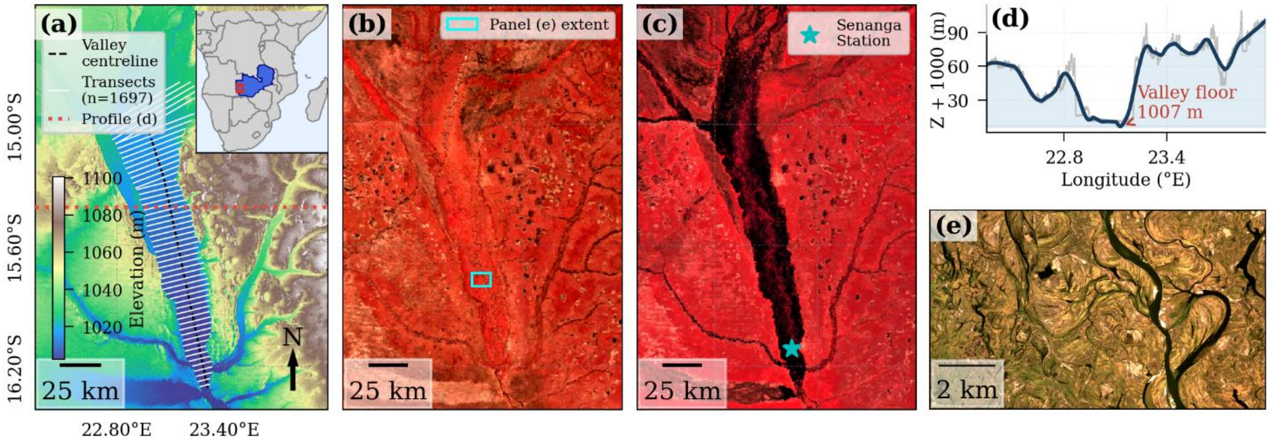

Fig. 1. (a) Detail of the 170 km long study reach showing valley centreline (dashed), and analysis transects (for clarity, not all are shown). Background: COP-DEM 30 m. River flow is north to south. Inset: Location of the upper Zambezi River, western Zambia. (b) Dry season (August 2025) and (c) wet season (March 2026) MODIS-terra 500 m false-colour-composites – dark = wet, red = vegetated. (d) Valley elevation profile (red dotted line in (a)). (e) Sinuous channel, scroll plains and oxbows providing evidence of lateral channel mobility (PlanetScope 3 m data).

Annual median NDWI composites were computed per pixel after QA_PIXEL cloud masking (36 years; 4 years had data gaps). The annual median was used to capture year-round channel signal while suppressing seasonal floodplain inundation. A raster-to-skeletonisation approach was used to extract a valley centreline from a valley polygon, followed by geometric smoothing to suppress local artefacts. Perpendicular transects were then generated at fixed along-valley spacing (100 m) on the centreline (Fig. 1a). Since our aim is to track lateral mobility, we chose valley (not channel) centreline because the channel centreline shifts from year to year.

III. Methodology

A. Gaussian Sub-Pixel Fitting

For each transect–year pair, NDWI values sampled at 30 m (Landsat resolution) intervals were fitted with

$$f(d) = B + A\,exp[-(d - C)^2/(2\sigma^2)] \quad (1)$$

where d is along-transect distance (m), B is the NDWI background, A is peak amplitude above background, C is the channel centre position, and σ is the Gaussian width parameter (Fig. 2a). The Gaussian approximates a PSF-convolved top-hat, representing spectral mixing [8] between the channel and the lower-wetness floodplain: the Gaussian approximation is exact for channels narrower than ~3 pixels (<90 m for Landsat) and remains close for wider channels. Fitting used nonlinear least squares. The background bound was set adaptively as $\hat{B} \pm$ 3·MAD (median absolute deviation of the profile, floored at 0.01 NDWI units to prevent bound collapse on near-uniform profiles). The 1σ positional uncertainty σ_pos is the square root of the covariance diagonal element corresponding to C; when the covariance matrix is degenerate, an analytical fallback $\sigma\_pos \approx (\sigma/\sqrt{N\_eff}) \cdot (1/A) \cdot (1/\sqrt{R^2})$ is applied, where $N\_eff = \max(2\sigma/\Delta x, 1)$ and R^2 is floored at 0.05 to prevent division collapse on near-zero fits and Δx is dx_eff (see §III.E).

B. Channel Width Detection

Two width estimates are produced. The Full Width at Half Maxima (FWHM = 2.355σ) is the analytical Gaussian width and the primary channel-width output. A physical width is derived from the inflection points of the Savitzky–Golay-smoothed NDWI profile within a ±3σ window centred on C; when inflections cannot be resolved, a fallback is measured at the Full Width at Tenth Maximum (FWTM; B + 0.1 × A). The offset of the physical midpoint from C (width_asymmetry_m) is also retained. For channels narrower than the sensor resolution limit (§III.E), both measures constitute upper bounds on true bankfull width due to PSF broadening.

Transects are oriented perpendicular to the valley centreline rather than to the channel centreline, so that all epochs share the same fixed cross-valley reference frame and lateral position change (ΔC) is a direct, rotation-free measure of cross-valley displacement. The reported widths are therefore *apparent*: when the local channel makes angle φ with the valley axis, $W_{\text{true}} = W_{\text{app}}\cos\,\varphi$. For low-sinuosity reaches ($\varphi \lesssim 15°$) the correction is less than 4% and negligible; for more sinuous reaches it can be applied where a channel centreline is available to estimate φ at each transect. Alternatively, if width accuracy is the primary objective rather than mobility tracking, channel-centreline-perpendicular transects can be substituted directly; all other processing steps are unchanged.

C. Multi-Thread Detection

A two-Gaussian candidate was considered when the NDWI profile exhibited at least two peaks (e.g., Fig. 2a) with a prominence threshold of max(min_amplitude, 4.5 × IQR), where IQR is the inter-quartile range of the profile. Of the two tallest detected peaks, a two-Gaussian model was attempted only when their prominence ratio exceeded 0.50 and their separation fell between dx_eff (see §III.E) and 60% of the total transect length.

The two-Gaussian model

$$f(d) = B + A_1\,exp[-(d - C_1)^2/(2{\sigma_1}^2)] + A_2\,exp[-(d - C_2)^2/(2{\sigma_2}^2)] \quad (2)$$

(7 free parameters) was accepted over (1) only when $\Delta BIC = BIC_1G - BIC_2G \geq 2.0$, corresponding to positive evidence [14]. The dominant thread (higher Gaussian mass $A \times \sigma$) is reported

as the primary position; the secondary thread position and mass are retained as auxiliary outputs. Multi-thread morphology (e.g. local division around islands; Fig. 2a) is recorded as a boolean braided_suspect field, decoupled from the quality flag, so a well-fit dual-thread reach can simultaneously carry flag = HIGH and braided_suspect = True.

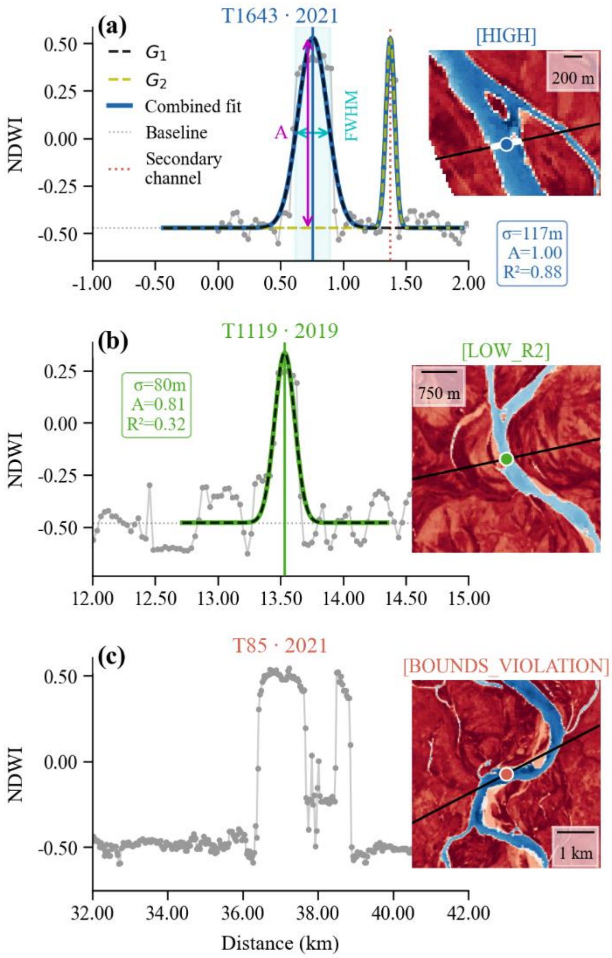

Fig. 2. Representative NDWI transect profiles (grey points), Gaussian fits, and Landsat NDWI maps for each quality flag class. Vertical line: channel centre. Lighter band: FWHM width. If detected, secondary channels are also marked. Gaussian fits: Amplitude (A), Full Width at Half Maxima (FWHM), and two channels, both Gaussian curves (G_1 & G_2) are also shown along with the combined curve (a). White line on NDWI map is channel width (= FWHM). In (b), R^2 is lower than used threshold (= 0.4) because of multiple NDWI peaks higher than the baseline (dotted line). In (c), Gaussian fitting failed as the transect is obliquely crossing the channel, resulting in a few kilometres wide channel, triggering quality control flag FAILED: BOUNDS_VIOLATION.

D. Temporal Continuity Window

To track progressive channel mobility rather than abrupt bend cutoff or avulsion events, two pre-regression screens remove position outliers before fitting. First, a position-envelope screen identifies transect-year observations whose centre position falls outside the per-transect median ±3·MAD computed from HIGH- and LOW-quality observations across the full record. Second, a step-rate screen flags year-on-year position changes (|Δcentre/Δyear|, m yr^{-1}) exceeding the per-transect median step rate by more than 4.5 × 1.4826 × MAD (approximately 4.5 robust standard deviations); the later of the two bounding observations is masked. Both screens add explicit boolean columns to the observation table rather than silently dropping rows, making every removal decision auditable. Using pre-regression cleaning rather than within-regression filtering preserves the pure-estimator structure of the OLS step and allows parallel fitting of all transect–year pairs independently.

E. Resolution-Aware Fit Quality Classification

Resolution-aware width thresholds. Rather than fixed sigma floors *for* initial Gaussian fitting parameters, the framework derives sensor- and geometry-specific thresholds from the effective along-transect sampling defined as: $dx\_eff = max(dx\_observed, p\ /\ (|cos\ \theta| + |sin\ \theta|), dx\_PSF)$, where dx_observed is the along-transect sample spacing (m), p is the nominal pixel size (30 m for Landsat), θ is the transect orientation angle measured from the UTM easting axis, and dx_PSF is an optional sensor PSF support radius (m; zero when not supplied). The middle term is the mean pixel-boundary crossing spacing for a transect at angle θ through a square pixel grid, equal to p at cardinal orientations and p/√2 ≈ 21 m at 45°. Two sigma thresholds follow from dx_eff and minimum effective FWHM sample counts n: σ = (n × dx_eff) / 2.355, with n = 1 defining σ_low (the minimum for a LOW-quality fit) and n = 2 defining σ_HQ (required for HIGH). For a 30 m Landsat transect, σ_HQ = (2 × 30) / 2.355 = 25.5 m, corresponding to a minimum HIGH-quality FWHM of 60 m (two pixels across the channel); σ_low = 12.7 m permits LOW-quality position recovery down to a one-pixel FWHM. Substituting p = 10 m for Sentinel-2 rescales all thresholds proportionally, making the formulation sensor-agnostic.

Quality classification. Fitted profiles are assigned one of three mutually exclusive flags (Fig. 2). **HIGH** requires all of: $R^2 \geq$ min_r2; amplitude $A \geq$ min_amplitude; SNR = A/noise_std ≥ 2.0; and σ_HQ ≤ σ ≤ max_sigma_m, where min_r2, min_amplitude, and max_sigma_m are user-supplied parameters (e.g., Fig. 2a). Fits failing any single condition are classified **LOW**, with a diagnostic reason flag identifying the cause: marginally resolved width below the HIGH gate (LOW_RESOLUTION, σ_low ≤ σ < σ_HQ); unresolved channel width (LOW_UNRESOLVED, σ < σ_low); weak amplitude (LOW_AMP); poor fit (LOW_R2; e.g., Fig. 2b); low SNR (LOW_SNR); or anomalously wide sigma suggestive of off-channel lock-on (LOW_WIDE, σ > 1.5 × typical_channel_sigma, applied as a post-classification override when the user supplies typical_channel_sigma "LOW flagged observations retain their centre position and enter mobility regression with their fitted σ_pos as the weight denominator (1/σ²), naturally down-weighting lower-quality fits: this is the mechanism enabling sub-pixel position recovery for channels below the formal resolution limit. **FAILED** covers three mutually exclusive conditions: CONVERGENCE_FAILED when the optimizer does not converge, BOUNDS_VIOLATION when initial parameter estimate falls outside bounds (e.g., Fig. 2c), and the pre-fit flat-signal (FLAT_SIGNAL) guard (profile IQR < 0.5 × min_amplitude), which rejects profiles lacking detectable spectral contrast before any fitting is attempted.

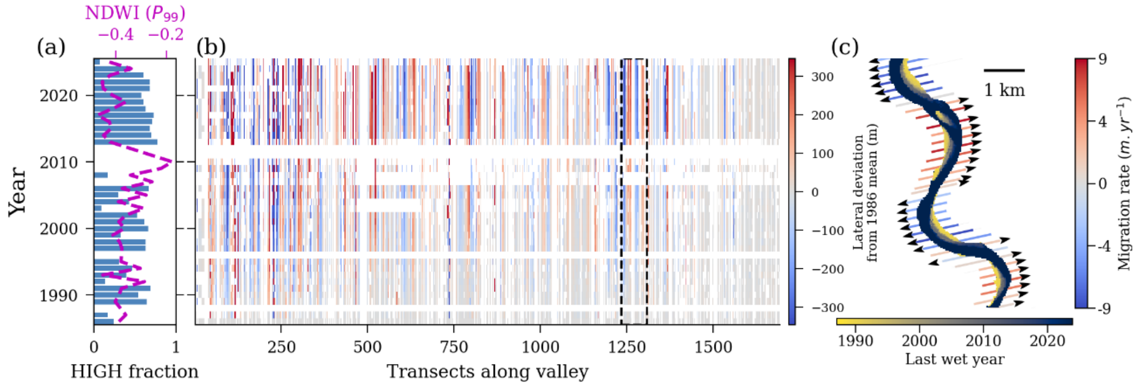

Fig. 3. (a) Fraction of HIGH flags per year and 99th percentile NDWI across all transect profiles per year. (b) Space–time diagram of lateral channel centre deviation from the 1986 baseline (m). Red: leftward (broadly east); blue: rightward (broadly west); Gray: LOW; white: NoData/FAILED. (c) Method validation: last wet year and channel mobility rate (lines with arrows) for a part of Zambezi River (for transects in dotted box in b) exhibiting lateral shifts. Mobility direction is shown by arrows. River flow is from north to south.

F. Mobility Rate Estimation

Mobility rate was estimated by weighted OLS regression of C(t) on year for observations with flag = HIGH or LOW, with weights $w_i = 1/\sigma^2\_pos,i$. σ_pos values were clipped to a minimum of 3 m (0.1 × the nominal Landsat pixel spacing), preserving the 3–12 m sub-pixel precision observed in the positional accuracy assessment and a maximum of $2 \times \sigma_{95}$, the 95th percentile positional uncertainty across the transect time series, to prevent sub-half-pixel weights from dominating the regression. Statistical significance was assessed by two-tailed t-test ($\alpha = 0.05$). Mobility rates are reported in the transect geometric coordinate system (positive toward the transect far end as digitised), which is consistent within each transect across all years but does not directly correspond to river-left or river-right mobility. As a non-parametric complement, a Mann-Kendall trend test and Theil-Sen slope estimator were also computed per transect. Transects were subsequently retained only if they passed both an ensemble-level MAD-based rate cap (median |rate| + 5 × 1.4826 × MAD) and showed directional signal by at least one criterion: weighted OLS $R^2 > 0.10$ or Mann-Kendall $p < 0.10$.

G. Model Parameters

We used a Gaussian-profile channel tracker with two parameter groups: calibrated detection thresholds, and fixed methodological defaults. Calibrated detection thresholds were minimum amplitude (min_amplitude), minimum fit quality (min_r2), maximum allowable Gaussian sigma (max_sigma_m), and when a priori channel dimensions are known – typical channel sigma (typical_channel_sigma). Fixed methodological defaults included BIC preference for one- vs two-Gaussian selection (bic_preference), and sensor-resolution controls (pixel_size, min_fwhm_samples_high, min_fwhm _samples_low, the optional transect_angle_deg, psf_support _m, min_channel_width_m).

IV. Results

A. Data Quality, Positional Uncertainty, and Model Sensitivity

Gaussian fitting yielded 61,092 transect–year records across 1,697 transects and 36 years (1986–2025). Of these, 46.0% were classified HIGH quality, 52.7% LOW. Ten of 36 years returned <30% HIGH-quality fits, coinciding with highly wet years in this floodplain (Fig. 3a). The flat-signal and convergence-failure rates (FAILED < 2%) confirm that the annual median composite effectively suppresses scene-level artefacts over the 36-year record.

After ensemble-level quality filtering (MAD-based rate cap, minimum trend signal), 1329 transects were retained, spanning the full 169 km reach with median transect spacing of 100 m and no gap exceeding 1.4 km (KS test vs. full dataset: $p = 1.00$, confirming spatial representativeness). For these transects, the median positional uncertainty across 22,126 HIGH-quality fits was σ_pos = 6.0 m (5th–95th percentile 4.0–11.5 m), approximately one-fifth of the 30 m Landsat pixel, confirming sub-pixel channel localisation. The median per-transect OLS rate standard error was 0.25 m/yr (IQR 0.13–0.53 m/yr).

We tested sensitivity on 85 randomly selected transects. Algorithm performance was stable across a 6× range of minimum amplitude (0.013–0.090) and a broad minimum R^2 range (0.10–0.55), with median channel width (281 m) and migration rate IQR (−5.6 to +5.2 m yr^{-1}) invariant to the R^2 threshold and insensitive to amplitude until detection rates decline above 0.09. The maximum channel half-width cap must exceed ~167 m to avoid fit collapse, and the native 30 m pixel size is essential: positional uncertainty grows by ~25% at 90 m and the algorithm yields no usable fits beyond ~150 m ground sampling distance.

B. Lateral Channel Mobility

Of the 1,329 retained transects, 1,227 (92%) exhibited statistically significant lateral mobility ($p < 0.05$, weighted OLS), corroborated by Mann-Kendall (1,167/1,329, 88%; median $|\tau| = 0.72$, IQR 0.43–0.89). Absolute migration rates spanned a wide range (IQR 1.1–6.1 m/yr; median 3.1 m/yr, 95% CI 2.8–3.4), with a long tail of rapidly migrating reaches up to 19.7 m/yr. OLS and Theil-Sen slopes agreed closely ($r = 0.96$; 98% same sign; median Theil-Sen 2.9 m/yr, 95% CI 2.7–3.1 m/yr), confirming robustness to parametric assumptions. Signed rates were approximately balanced (640 positive, 587 negative; Fig. 3b), consistent with the alternating-bend planform. Accordingly, reach-scale signed net displacement was statistically indistinguishable from zero (median 6 m, 95% CI −6–10 m), yet median absolute net displacement was 109 m (95% CI 101–118 m) from 1986-2025, confirming that individual reaches undergo sustained unidirectional migration, with opposing directions alternating along the planform. Migration directions are in visual agreement with channel position shifts in Fig. 3c, including near-zero rates at meander inflection points.

C. Channel Width and Geometry

Across 22,126 HIGH-quality observations, the median Gaussian FWHM was 260 m (IQR 205–344 m) and median physical width 258 m (IQR 215–324 m), mutually consistent and in agreement with the typical bankfull width of 250–350 m visible in Google Earth high-resolution imagery. Width trends were negligible at the reach scale (median FWHM trend −0.07 m/yr), with widening and narrowing reaches approximately balanced (628 vs. 701). Width asymmetry which is the signed offset of the physical channel midpoint from the Gaussian centre, had a reach-median of 0.0 m (95% CI −0.3–0.4 m; IQR −3.3–3.4 m), with near-equal numbers of left- and right-offset transects (664 vs. 665). Asymmetry trends were negligible (median 0.000 m/yr) and poorly constrained ($R^2 > 0.3$ at only 28 transects), indicating no systematic bank-side preference for erosion or accretion at the reach scale. The non-zero local asymmetry values at individual transects are consistent with the expected bank-alternation pattern at meander bends, where the outer bank erodes and the inner bank accretes asymmetrically.

V. Discussion

The annual median NDWI composite we adopted is a robust estimator of central tendency that suppresses scene-level artefacts (e.g., cloud contamination, atmospheric variability, bidirectional reflectance effects) without requiring stage-specific image selection. Unlike higher-order percentiles or maxima, which preferentially capture peak inundation and amplify transient floodplain expansion, the median provides a temporally stable, noise-resistant representation of valley-scale hydro-spectral regime. Within this framework, the subsequent Gaussian decomposition operates on a consistent annual signal, enabling repeatable sub-pixel separation of the channel mode from the broader floodplain background.

Compared to RivMAP [3] and RivaMap [4], the key advantage is applicability to channels occupying as few as 1–3 pixels and positional uncertainty tracking. We directly fit the spectral mixing profile rather than skeletonising a binary water mask; skeletonisation requires ≥8 pixels of channel width. Additionally, we provide an explicit per-observation positional uncertainty that propagates into the mobility rate estimate via weighted regression, rather than computing uncertainty post-hoc from ensemble variability.

VI. Conclusion

Our framework is immediately applicable to any river system for which a valley polygon can be delineated. Therefore, PyRiverShift could support a global lateral channel mobility dataset. A 40-year, globally consistent, sub-pixel channel mobility dataset from the Landsat archive, produced using PyRiverShift, would provide the empirical foundation to address some fundamental questions. In which sorts of physiographic settings are mobility rates highest and lowest? Is slow lateral mobility a stable state or a precursor to short-lived phases of more rapid mobility, perhaps involving threshold crossing? How do mobility rates adjust to interannual climate variability, such as ENSO-driven shifts in flood frequency and magnitude? The answers to these sorts of questions have implications for many academic disciplines, engineers and planners; for example, lateral mobility rates set the pace of floodplain habitat turnover and govern the geometry of alluvial stratigraphy, control the delivery of terrestrial organic carbon to river systems, and determine bank-erosion hazard timescales. Immediate extensions to our framework include reach-scale threshold prediction, systematic mapping of the most-to-least laterally active reaches as a bank-erosion hazard layer, canopy occlusion, and integration with Sentinel-2 to extend sub-pixel detection to channels narrower than one Landsat pixel.

Acknowledgment

MS is a Newton International Fellow, funded by the Royal Society, London, and gratefully acknowledges the support. MS also acknowledges Courtney Goode for discussions.

References

[1] M. Donovan, P. Belmont, B. Notebaert, T. Coombs, P. Larson, and M. Souffront, "Accounting for uncertainty in remotely-sensed measurements of river planform change," *Earth-Science Reviews,* vol. 193, pp. 220–236, 2019.

[2] J. A. Constantine, T. Dunne, J. Ahmed, C. Legleiter, and E. D. Lazarus, "Sediment supply as a driver of river meandering and floodplain evolution in the Amazon Basin," *Nat. Geosci.,* vol. 7, pp. 899–903, 2014.

[3] J. Schwenk, A. Khandelwal, M. Fratkin, V. Kumar, and E. Foufoula-Georgiou, "High spatiotemporal resolution of river planform dynamics from Landsat: The RivMAP toolbox and results from the Ucayali River," *Earth and Space Science,* vol. 4, pp. 46–75, 2017.

[4] F. Isikdogan, A. Bovik, and P. Passalacqua, "RivaMap: An automated river analysis and mapping engine," *Remote Sens. Environ.,* vol. 202, pp. 88–97, 2017.

[5] X. Yang, T. M. Pavelsky, G. H. Allen, and G. Donchyts, "RivWidthCloud: An Automated Google Earth Engine Algorithm for River Width Extraction From Remotely Sensed Imagery," *IEEE Geosci. Remote Sens. Lett.,* vol. 17, pp. 217–221, 2020.

[6] J.-F. Pekel, A. Cottam, N. Gorelick, and A. S. Belward, "High-resolution mapping of global surface water and its long-term changes," *Nature,* vol. 540, pp. 418–422, 2016.

[7] G. W. Nagel, S. E. Darby, and J. Leyland, "The use of satellite remote sensing for exploring river meander migration," *Earth-Science Reviews,* vol. 247, p. 104607, 2023.

[8] Q. Wang, C. Zhang, X. Tong, and P. M. Atkinson, "General solution to reduce the point spread function effect in subpixel mapping," *Remote Sens. Environ.,* vol. 251, p. 112054, 2020.

[9] S. K. McFeeters, "The use of the Normalized Difference Water Index (NDWI) in the delineation of open water features," *Int. J. Remote Sens.,* vol. 17, pp. 1425–1432, 1996.

[10] G. Schwarz, "Estimating the Dimension of a Model," *The Annals of Statistics,* vol. 6, pp. 461–464, 1978.

[11] A. M. Banda, K. Banda, E. Sakala, M. Chomba, and I. A. Nyambe, "Assessment of land use change in the wetland of Barotse Floodplain, Zambezi River Sub-Basin, Zambia," *Nat. Hazards,* vol. 115, pp. 1193–1211, 2023.

[12] M. Lourenco *et al.*, "Assessment of source regions of the Zambezi River: implications for regional water security," *Hydrol. Earth Syst. Sci.,* vol. 29, pp. 4557–4583, 2025.

[13] *WetlandMapper: A Python package for automatic wetland mapping, dynamics classification, and cover-type characterisation*. (2026), doi: https://doi.org/10.5281/zenodo.18967176.

[14] A. E. Raftery, "Bayesian Model Selection in Social Research," *Sociological Methodology,* vol. 25, pp. 111–163, 1995.